

Towards spin state tailoring of charged excitons in InGaAs quantum dots using oblique magnetic fields

K. Barr ¹, B. Hourahine ¹, C. Schneider ², S. Höfling ³, and K. G. Lagoudakis ¹

¹*SUPA, Department of Physics, University of Strathclyde, Glasgow G4 0NG, United Kingdom*

²*Carl von Ossietzky Universität Oldenburg, 26129 Oldenburg, Germany*

³*Julius-Maximilians-Universität Würzburg, Physikalisches Institut, Lehrstuhl für Technische Physik, Am Hubland, 97074 Würzburg, Deutschland*



(Received 2 May 2023; revised 2 February 2024; accepted 6 February 2024; published 27 February 2024)

We investigate the effect of oblique magnetic field configurations on a singly charged self-assembled quantum dot system as a means to tune the spin composition of the ground electron spin eigenstates. Using magneto-optical spectroscopy and Stokes polarimetry techniques, we evaluate the anisotropic g factors and characterize the polarization properties of the charged quantum dot system under oblique fields. We compare the results to a simple model that captures the resulting level structure and polarization selection rules for arbitrary magnetic field orientations. Under oblique magnetic fields, the system's ground spin eigenstates are composed of unequal superpositions of the electron spins. This provides an additional degree of freedom to tailor the composition of the ground spin states in charged quantum dots and based on this we demonstrate spin pumping and initialization of the tailored ground states, confirming that the double- Λ level structure of the charged quantum dot persists in oblique magnetic fields. These combined results show that the uneven weightings of the tailored spin states can yield systems with interesting behaviors, with a potential towards developing spin-selective readout schemes to further enhance the capabilities of spin qubits.

DOI: [10.1103/PhysRevB.109.075433](https://doi.org/10.1103/PhysRevB.109.075433)

I. INTRODUCTION

Self-assembled semiconductor quantum dots (QDs) provide an excellent arena for improving our fundamental knowledge of solid-state systems while additionally demonstrating viability for future quantum hardware [1]. This combination of a physics-rich environment linked with potential for future applications [2], makes research into such systems both relevant and exciting.

Generally, the optical and electronic properties of QDs result from the chemical composition, physical shape, and strain, as well as the type of excitonic complexes [3–5] and interactions with the nuclear spins of the surrounding environment [6], just to name a few.

The study of charged quantum dots under external magnetic fields enables access to the spin states of electrons and holes with the Faraday configuration (field parallel to growth axis) typically used for the spin preserving cyclic transitions or the Voigt configuration (field perpendicular to growth axis) for the optically addressable double- Λ system [7]. Understanding the magneto-optical properties of a quantum dot requires characterization of the g -factor tensors.

Magnetic fields that are applied with varying angles in the plane perpendicular to the growth axis enable the

characterization of the anisotropy of the in-plane g factors. Combining these measurements with magnetic fields out-of-plane allows for the estimation of the complete g -factor tensor of QDs. This is typically done via the application of magnetic fields in oblique angles using in parallel additional techniques ranging from photoluminescence polarimetry [8–15], pump-probe Faraday rotation [16–19], and resonant spin amplification [20] to spin-noise spectroscopy [21], magnetotunneling [22,23] and magnetocapacitance [24].

Oblique magnetic fields applied on quantum dots additionally enable access to dark exciton states and recent works have focused on their dynamics [25] and their interactions with strong optical fields [26]. Tilted fields have also been used for the in-depth study of impurities in quantum dots [27,28] and for the investigation of spin-flip Raman scattering [29,30].

In this work, we show that by transitioning towards oblique magnetic field angles (containing both B_z and B_x components), a double- Λ level structure is retained yet the ground spin states are now formed from unequal superpositions of spins. From this we see the unique capability of tailoring the ground spin state composition, while also combining elements of both Voigt and Faraday configurations.

Through a series of experiments in both Voigt and oblique configurations we evaluate the anisotropic electron and hole g -factor components and characterize polarization properties of the emission spectra; these are then used to confirm a descriptive model of the system. Finally, we show spin pumping and spin initialization of the ground spin states in an oblique magnetic field with behavior similar to the Voigt configuration, confirming that oblique magnetic field configurations

Published by the American Physical Society under the terms of the Creative Commons Attribution 4.0 International license. Further distribution of this work must maintain attribution to the author(s) and the published article's title, journal citation, and DOI.

produce a coupled level structure that can also be used for all-optical coherent control.

This paper is organized as follows: In Sec. II we introduce the model and simulated results of transition strengths, spin-state compositions, and polarization properties of the target QD along with the experimental setup and methods used. Section III presents the experimental findings used to characterize the system's level structure and behavior, culminating in the demonstration of spin pumping in an oblique field configuration and its comparison to spin pumping in the Voigt configuration. Finally, a discussion and our conclusions are presented in Sec. IV.

II. THEORY AND METHODS

A. Hamiltonians, eigenstates, and spin-state weights

The electronic states of a charged quantum dot are subject to the Zeeman interaction in the presence of a magnetic field. Due to the additional confined charge they are known to exhibit no exchange interaction [8]. To simulate the behavior of the charged QDs in oblique magnetic fields, we treat both electrons and trions (holes) as pseudospins; the electrons as spins $\hat{J}_e = \pm 1/2$, and the trions as spins $\hat{J}_h = \pm 3/2$ associated with the heavy-hole (hh) states. Here, preselection of the quantum dots allows us to neglect light-hole (lh) states and hh-lh mixing. The Zeeman interaction Hamiltonian for both electrons and heavy holes within the QD is given by

$$\hat{H}_{e/h} = -\mu_B \sum_{\alpha \in x,y,z} g_{e/h}^{\alpha} \cdot \mathbf{B}_a \hat{S}_a, \quad (1)$$

where μ_B is the Bohr magneton, $g_{e/h}^{\alpha}$ are the electron/hole g factors, \mathbf{B}_a is the applied magnetic field vector components, and \hat{S}_a are the Pauli spin operators.

For the hole states $\hat{J}_h = \pm 3/2$ and we use the Luttinger-Kohn Hamiltonian with the valence-band parameters κ_{α} and q_{α} , akin to Bayer *et al.* [8] and other works [10,12]. By introducing the heavy-hole subspace matrices for \hat{J}_{α} and \hat{J}_{α}^3 the hole Hamiltonian can be reduced to a form similar to Eq. (1), containing the same spin operators and an effective hole g factor while differing only by a sign prefactor. In the presence of hh-lh mixing the full \hat{J}_h matrices with additional parameters relating to the mixing ratio would be required, at which point the process may then be better described using the full Luttinger-Kohn and Bir-Pikus Hamiltonian [12,31]. Here however, we can simplify the model as we have preselected the quantum dot we study for minimal hh-lh mixing [32].

The Hamiltonian (1) can be readily diagonalized for both electrons and holes and allow us to understand the quantum dot's response to an applied magnetic field in arbitrary orientations. A schematic diagram of the system is shown in Fig. 1(a) which consists of the electronic ground states, $|\downarrow\rangle_{\theta}$ and $|\uparrow\rangle_{\theta}$, and excited trion states, $|\downarrow\uparrow\downarrow\rangle_{\theta}$ and $|\uparrow\downarrow\uparrow\rangle_{\theta}$. Here, \downarrow, \uparrow represent the ground state electron spins while \downarrow, \uparrow relate to the hole spins. The excited trion states consist of two electrons with opposite spins (in a singletlike spinless state) and a hole that interacts with the magnetic field. The trion states can therefore be described in a simpler way only considering the contributions of the heavy hole spins.

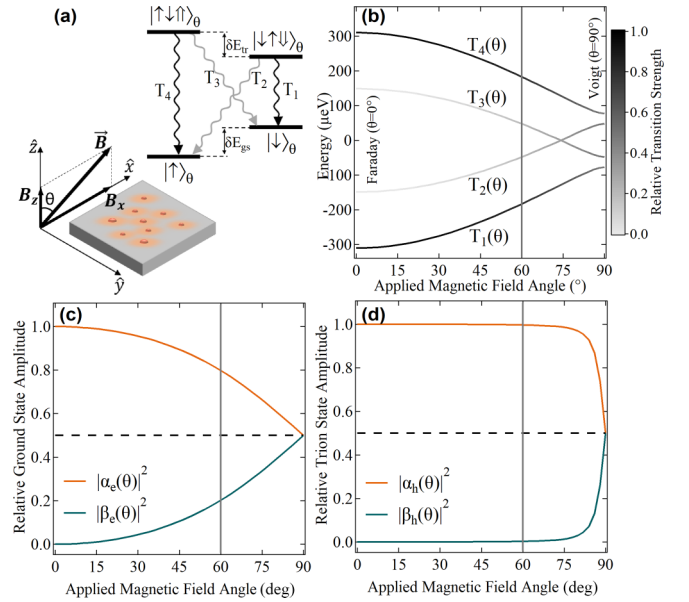


FIG. 1. (a) Top: Schematic diagram of the double- Λ level structure found within oblique and Voigt configurations. Bottom: Simplified view of structure depicting the QDs inside the sample (top and bottom distributed Bragg reflectors are not shown) with the principal Z-axis. (b) Simulated results of a charged QD four-level splitting (T_1 - T_4) as a function of applied magnetic field angle ($B_0 = 5$ T) using g factors extracted from experimental data. The color bar indicates relative transition intensity for each transition. (c) Amplitude square of the normalized ground state basis weights $\alpha_e(\theta)$ and $\beta_e(\theta)$ as a function of applied field angle. These are components of the ground state eigenstates generated in a nonzero magnetic field. When $\theta < 90^\circ$ we see an unequal weighting of the basis spin between the two ground states. (d) Amplitude square of the normalized trion states basis weights $\alpha_h(\theta)$ and $\beta_h(\theta)$, as a function of applied field angle. Again, as we move away from the Voigt configuration the trions have a nonequal basis hole spin weight.

Under an external applied magnetic field, both ground and excited trion states split because of the Zeeman interaction by δE_{gs} and δE_{tr} respectively and a four-level structure like the one shown in Fig. 1(a) appears. The resulting spin eigenstates are composed of weighted superpositions of the basis states aligned along the z axis ($\theta_z = 0^\circ$) which are either $|\downarrow\rangle_z$ or $|\uparrow\rangle_z$ for the ground state electrons, or $|\downarrow\uparrow\downarrow\rangle_z$ and $|\uparrow\downarrow\uparrow\rangle_z$ for the excited state trions. This allows us to express the QD eigenstates as a linear combination of the basis states. Thus, the eigenstates of both the ground and trion states can be written as

$$\begin{aligned} |\uparrow\rangle_{\theta} &= \alpha_e(\theta)|\uparrow\rangle_z - \beta_e(\theta)|\downarrow\rangle_z, \\ |\downarrow\rangle_{\theta} &= \beta_e(\theta)|\uparrow\rangle_z + \alpha_e(\theta)|\downarrow\rangle_z, \\ |\uparrow\downarrow\uparrow\rangle_{\theta} &= \alpha_h(\theta)|\uparrow\downarrow\uparrow\rangle_z - \beta_h(\theta)|\downarrow\uparrow\downarrow\rangle_z, \\ |\downarrow\uparrow\downarrow\rangle_{\theta} &= \beta_h(\theta)|\uparrow\downarrow\uparrow\rangle_z + \alpha_h(\theta)|\downarrow\uparrow\downarrow\rangle_z. \end{aligned} \quad (2)$$

The terms $\alpha_{e/h}(\theta)$ and $\beta_{e/h}(\theta)$ in (2) are the normalized weights found by explicitly solving for the eigenvectors of the Hamiltonian (1).

The complete expressions of the terms $\alpha_{e/h}(\theta)$ and $\beta_{e/h}(\theta)$ in Eq. (2) along with the normalization factor are given in (3):

$$\alpha_{e/h}(\theta) = \frac{1}{N_{e/h}(\theta)} [g_{e/h}^z \cos(\theta) + \sqrt{[g_{e/h}^z \cos(\theta)]^2 + [g_{e/h}^x \sin(\theta)]^2}], \quad \beta_{e/h}(\theta) = \frac{g_{e/h}^x \sin(\theta)}{N_{e/h}(\theta)},$$

$$N_{e/h}(\theta) = 2[(g_{e/h}^z \cos \theta)^2 + (g_{e/h}^x \sin \theta)^2 + g_{e/h}^z \cos \theta - \sqrt{(g_{e/h}^z \cos \theta)^2 + (g_{e/h}^x \sin \theta)^2}]. \quad (3)$$

The sample orientation and axis choice used with respect to the QD sample are shown in the bottom inset of Fig. 1(a), with the z axis aligned along the growth axis.

Figure 1(b) shows simulated eigenenergies of the four available transitions between the eigenstates of a charged QD ($B_0 = 5$ T) as a function of applied magnetic field angle θ . In the same figure, the strength of each transition dipole is represented by the line color. In the Faraday configuration ($\theta = 0^\circ$), the two inner transitions are entirely inactive while in the Voigt configuration all four transitions are equally optically active. In terms of energy splittings, as θ moves from Faraday to Voigt configurations, there is a reduction because of the difference of the g factors in Voigt and Faraday configurations. Interestingly, there is an observed level crossing at $\theta = \sim 74^\circ$ between transitions $T_2(\theta)$ and $T_3(\theta)$ which aligns well with experimental observations in oblique ($\theta_{\text{obl}} = 60^\circ$) and Voigt ($\theta_V = 90^\circ$) configurations as shown further on. At $\theta_{\text{obl}} = 60^\circ$, the model predicts that the ratio of the emission intensity of the inner to outer transitions is ~ 0.3 .

The normalized weights of the basis electron spins in the ground states are shown in Fig. 1(c) while the normalized weights of the basis hole spins in the excited states are shown in Fig. 1(d). In both cases, there is a clear dependence on the magnetic field angle θ : at $\theta_F = 0^\circ$ (Faraday configuration), we retrieve pure spin-up and spin-down basis states while at $\theta_V = 90^\circ$ (Voigt configuration), we see equally weighted basis state contributions. By transitioning towards oblique configurations, it is clear that the eigenstates are formed of unequal weights which shows that using an external magnetic field at an oblique angle allows for precise tailoring of the spin-up and spin-down components in the resultant electronic ground and excited states.

B. Effective polarizations

Previous research has highlighted that polarization properties of charged QDs in oblique magnetic fields differ significantly from the Voigt configuration [14]. To further shed light on this behavior we characterized the polarization state of QD emission through Stokes polarimetry. The Stokes vector \mathbf{S} consists of the four Stokes parameters, $\mathbf{S} = [S_0, S_1, S_2, S_3]$, relating to the intensity of light, and degree of linear, diagonal, and circular polarization respectively and proves a convenient method for the complete characterization of a polarization state of light [33,34]. Evaluating the Stokes parameters from theory alongside development of a Stokes polarimetry setup allows for direct comparisons between theory and experiment to be made. Each Stokes vector was evaluated from the transition dipole matrix elements of the optical transitions. The transition dipole matrix element between an initial and final state evaluated as $\langle f|\mu|i\rangle$ [31,35] yields a complex electric field amplitude $\vec{\epsilon}$, from which

relative transition strength is found as shown in Fig. 1(b). The Stokes parameters are then represented by the square of the amplitudes and are evaluated from $\vec{\epsilon}$ using the following expressions:

$$S_0 = |\epsilon_x|^2 + |\epsilon_y|^2, \quad S_1 = |\epsilon_x|^2 - |\epsilon_y|^2,$$

$$S_2 = 2\text{Re}(\epsilon_x \epsilon_y^*), \quad S_3 = -2\text{Im}(\epsilon_x \epsilon_y^*). \quad (4)$$

To get the normalized Stokes parameters, we take S_i/S_0 yielding the normalized polarization components (S_1, S_2, S_3) which vary between -1 and 1 , dependent upon the degree of the polarization component. The degree of polarization (DOP) can be calculated from the individual stokes parameters in (4) by taking $\text{DOP} = \sqrt{S_1^2 + S_2^2 + S_3^2}/S_0$ and it is 1 for all transitions in our simulations.

The simulated results of the normalized linear (S_1) and circular (S_3) parameters are shown as a function of field angle θ in Figs. 2(a)–2(d) for each transition. Because of the chosen symmetry of the simulated system, the diagonal (S_2) component was 0 for all magnetic field angles and thus was not displayed. The maximal values of $|S_1| = 1$ in the Voigt configuration ($\theta_V = 90^\circ$) and $|S_3| = 1$ in the Faraday

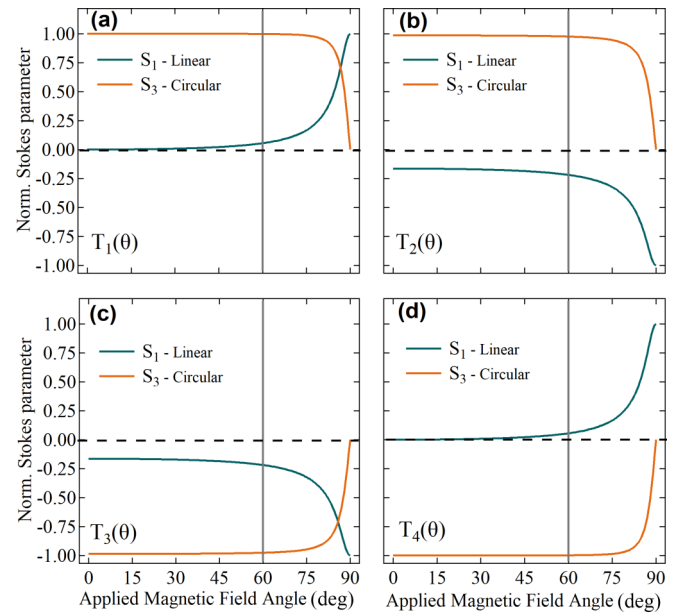


FIG. 2. (a)–(d) Simulated polarization of light emitted from each transition (as seen in Fig. 1) as a function of applied magnetic field angle ($B_0 = 5$ T). We show only the linear (S_1) and circular (S_3) component of the Stokes vector as no diagonal component ($S_2 = 0$) is observed. These simulations predict that a small fraction of linear S_1 component remains in both (b) T_2 and (c) T_3 across all angles, however the optical activity of these two transitions drops to zero for low magnetic field angles.

($\theta_F = 0^\circ$) correctly match expectations. Of interest here, and overlooked in previous works, are transitions $T_2(\theta)$ and $T_3(\theta)$ which maintain some degree of linearity even under oblique angles near the Faraday configuration. Both transitions however become optically inactive at low angles.

C. Experimental details and methods

The self-assembled, δ -doped, InGaAs QD sample emits in the region 910–920 nm and was grown by the Stranski-Krastanow method at the center of a GaAs microcavity [36,37] A single layer of InAs QDs was deposited on the substrate and capped with a 100-nm GaAs layer. At 10 nm below the QD layer a high-density ($\sim 10^{11} \text{ cm}^{-2}$) δ -doped region of silicon exists to greatly increase the probability of charged QDs, resulting in approximately one-third of the QDs being in a charged state, confirmed through fourfold symmetric level splitting in high magnetic fields under the Voigt configuration.

The sample is housed within a continuous flow liquid helium magnetic cryostat (Oxford Microstat-MO) that has been combined with a helium cryorecirculator (Coldedge Stinger) for closed-cycle operation [38] and can apply a homogeneous magnetic field of up to 5 T directly through the central axis of the sample chamber. The sample is maintained at approximately 6.8–7 K over the course of all experiments. Copper sample holders with embedded 45° silver-coated prisms were designed to allow for magnetic field application in either the Voigt configuration, or in the oblique configuration $\theta_{\text{obl}} = 60^\circ$ with respect to the z axis as shown in the top and bottom right-side insets in Fig. 3(a).

To enable relocating the QD used here when switching between different configurations, we use features of an aluminum mask deposited on the sample in combination with the spectral signature of this QD at zero and maximum magnetic field.

Figure 3(a) shows a schematic of the experimental setup used for the measurements. Optical excitation was done either above-band (Ab.bd laser), with a 780-nm diode laser, or resonant (Res. laser), using a tunable single-mode Ti:sapphire laser. Each are introduced through a polarization maintaining fiber, before passing a combination of a linear polarizer (LP), quarter-wave plate ($\lambda/4$) and half-wave plate ($\lambda/2$), yielding full control over the polarization of incident light. Monitoring of the resonant laser frequency is achieved in real time using a Fizeau-type wavemeter with 10 MHz frequency resolution.

To optically address individual QDs, a confocal microscopy setup allows for both excitation and detection through a 0.5 NA long working distance (~ 12 mm) microscope objective lens. The excitation spot for both the resonant and above-band lasers is of the order of $\sim 1 \mu\text{m}$ full width at half maximum. Polarization-resolved spectroscopy was performed by filtering photoluminescence using a custom rotating quarter-wave plate (QWP) polarimetry setup inspired by other works [39]. This consists of the motorized quarter-wave plate ($m-\lambda/4$) and the polarizing beam splitter (PBS) as shown in Fig. 3(a). The additional motorized half-wave plate ($m-\lambda/2$) can be removed and when present, enables cross-polarized reflectivity, rejecting back-reflected laser light that is present during resonant experiments such as spin pumping presented in Sec. III.

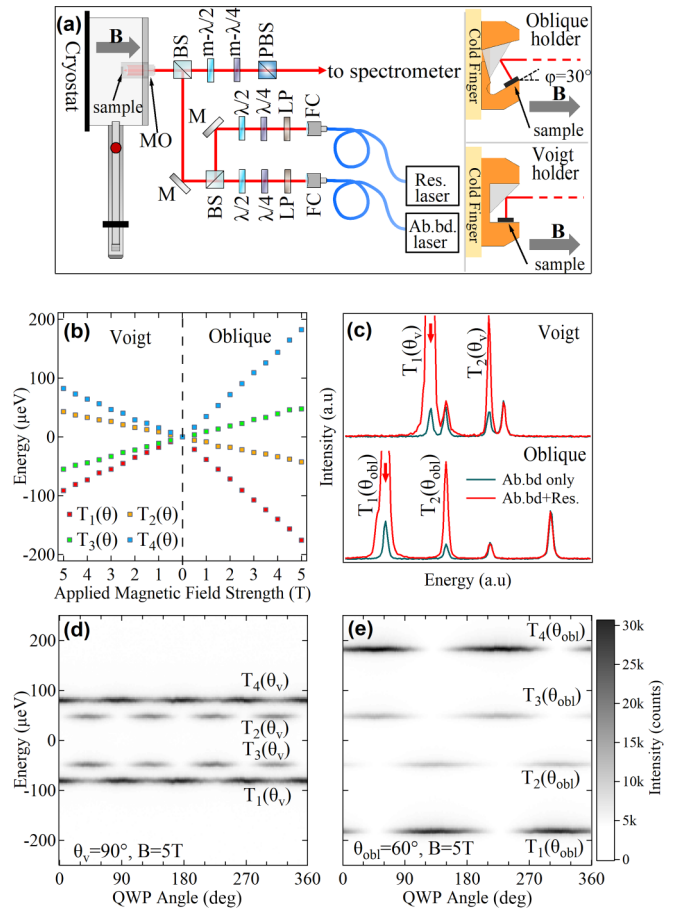


FIG. 3. (a) Schematic diagram of the experimental setup with top-right (bottom-right) inset: oblique (Voigt) field sample holder. The excitation setup consists of a combination of an above-band laser (Ab.bd) and a resonant laser (Res.) with complete polarization control. Excitation and light collection are done through a 0.5 NA microscope objective (MO). The emission is spatially filtered and sent to the spectrometer. M: mirror, FC: fiber coupler, LP: linear polarizer, (P)BS: (polarizing) beam splitter, and $m-\lambda/2(4)$: motorized half (quarter) wave plate. (b) Zeeman splitting of the QD as a function of magnetic field strength in the Voigt (left) and 60° oblique (right) configuration. T_2 and T_3 exchange relative positions between configurations. (c) Confirmation of the exchanged position in (b) via resonant excitation on T_1 (red arrows) which shows increased emission on either the third peak location [$T_2(\theta_v)$] or the adjacent second location [$T_2(\theta_{\text{obl}})$] because of spin pumping. (d),(e) Rotating quarter wave plate polarimetry of target QD in Voigt and oblique configuration respectively. The intensity profiles seen for the Voigt configuration are indicative of highly linear emission whereas for the oblique case they show high degree of circularity.

When implementing a QWP polarimetry setup it is important to investigate how optical elements prior to the polarimeter may affect the polarization of incident light reflected/transmitted through. Thus, the optical elements between the QD sample and the QWP polarimeter were characterized by measuring a laser with known polarizations before and after the elements which allowed us to construct an inverse Mueller matrix corresponding to the overall effect of these particular optical elements [40]. This is then introduced

as a correction, allowing for improved accuracy of the polarimeter. The photoluminescence was then spectrally filtered through a custom-built double (2×1 m long) Czerny-Turner spectrometer with $\sim 8 \mu\text{eV}$ resolution, before detection of either wavelength spectra on a charge-coupled device array, or photon count rates at a particular energy via a single-photon counting module.

III. RESULTS

A. Characterization of level structure

The fourfold splitting of singly charged excitons in the Voigt configuration leads to a double-lambda system that allows for the evaluation of the in-plane g factors in a straightforward manner. In this configuration, ground and excited state splitting are a result of only the in-plane electron and hole g -factor components g_e^x and g_h^x , which can be readily obtained from experiment. Measurements of level splitting and polarization-resolved photoluminescence were taken under above-band excitation with power in the range 250 ± 50 nW throughout data collection. This excitation power corresponds to only 20–40% of the saturation power for this quantum dot ($P_{\text{sat}} = 740 \pm 20$ nW) and ensured high-count rates while maintaining a narrow transition linewidth. The saturation power value was found by performing intensity dependent photoluminescence measurements on the target QD, with further information and data provided in the Supplemental Material [41].

In Fig. 3(b) we show level splitting in both the Voigt (left) and oblique (right) configuration as a function of applied magnetic field strength after diamagnetic shift removal. The QD experiences a diamagnetic shift proportional to the square of the applied field alongside this linear Zeeman splitting. The Voigt diamagnetic shift factor was found to be $\alpha_V = 4.67 \mu\text{eV}/T^2$, while the oblique configurations diamagnetic shift factor was $\alpha_{\text{obl}} = 6.14 \mu\text{eV}/T^2$. From the Zeeman splitting data at various field strengths, the in-plane g factors were evaluated as $|g_e^x| = 0.442 \pm 0.005$ and $|g_h^x| = 0.111 \pm 0.004$.

Transitioning towards the oblique configuration ($\theta_{\text{obl}} = 60^\circ$) in Fig. 3(b) (right) shows similar fourfold splitting, but with a greater magnitude of relative separation between the transitions. The contribution of both in-plane and out-of-plane g -factor components, as opposed to in-plane only, intuitively confirms this behavior should be common. At $B_0 = 5$ T, we see an average threefold increase in the separation between adjacent transitions with respect to the splittings in the Voigt configuration. Immediate benefits of working in oblique configurations can be seen; as to obtain similar separation to the Voigt at 5 T, the field strength can be as low as 2 T. Simply lowering the requirement on the magnetic field strength to obtain sufficient splitting allows for the field strength to be more freely adapted towards improving and extending coherence properties of the system. Using the previously extracted in-plane g -factor components alongside the oblique measurements, out-of-plane g -factor components were evaluated as $|g_e^z| = 0.505 \pm 0.032$ and $|g_h^z| = 1.575 \pm 0.023$.

Noting the location of transitions T_1 - T_4 in the two different configurations, we see that $T_2(\theta)$ and $T_3(\theta)$ exchange

position between the Voigt and oblique configuration. Figure 1(b) shows that level crossing between T_2 and T_3 takes place at $\theta = \sim 74^\circ$ which lies in-between the two magnetic field configurations used in this work. Figure 3(c) demonstrates the experimental technique used for confirmation whereby combining above-band and resonant excitation on the lowest energy outer transition (T_1 , left) reveals the lambda-coupled T_2 inner transition, showing increased emission because of spin pumping. Here the increased emission comes either from the adjacent (lowest energy) inner transition when the magnetic field is applied at $\theta_{\text{obl}} = 60^\circ$, or at the highest energy inner transition when the magnetic field is applied at $\theta_V = 90^\circ$. This observation shows that in both cases we are observing the same lambda-coupled pair (T_1 , T_2), but because of the different ground and excited level splittings in the two configurations, the emission energy is modified and the two inner transitions switch order.

Polarization-resolved spectroscopy using QWP polarimetry is shown in Figs. 3(d) and 3(e) for the Voigt and oblique configurations respectively. The quarter-wave plate is rotated over 360° with a 2° step and a complete spectrum of the photoluminescence is acquired for each waveplate angle. A multi-Lorentzian peak fit is used for each spectrum with a common offset and linewidth for all four peaks. Using the fitted peak parameters, we calculate the overall intensity (peak area) of each transition for all QWP angles γ , resulting in an intensity line profile $I_n(\gamma)$ with $n \in [1, 4]$ the transition number. Using this intensity profile, the associated Stokes vector could then be evaluated [34].

Figure 3(d) shows the QWP polarimetry in the Voigt configuration. This pattern is indicative of a near unity value for the linear component S_1 and is expected in this geometry. Here, the copolarized pairs can be seen to be the outer transitions (T_1 , T_4) and the inner (T_2 , T_3) transitions by observing the similar intensities as a function of QWP angle.

Conversely, Fig. 3(e) shows the polarimetry data in the oblique configuration, indicating that the copolarized pairs are (T_1 , T_2) and (T_3 , T_4). This is influenced by the high degree of right and left circular polarization that dominates heavily at oblique angles as was shown in the simulated polarization properties in Fig. 2. A comparison between the experimentally evaluated Stokes parameters and those calculated from the simulations in the oblique configuration is shown in Table I. The circular S_3 components appear similar, while the linear S_1 components show a small discrepancy compared to simulated values. The S_2 component is below 1.5% for all four transitions. This aside, the overall behavior of the linear components is consistent in that the inner transitions exhibit a higher, shared degree of linearity. All four transitions showed a near unity degree of polarization (DOP). The relative transition strengths are calculated by taking the ratio of S_0 for the inner transitions with respect to the corresponding outer transition for each pair T_1 - T_2 and T_3 - T_4 and show a good agreement with the simulated results.

B. Spin pumping in an oblique configuration

The fourfold splitting we see in oblique magnetic fields implies that a coupled double- Λ structure should be in operation. Using this assumption, we were able to identify the

TABLE I. Normalized Stokes parameters and degree of polarization comparison at $\theta_{\text{obl}} = 60^\circ$. All four transitions show a DOP of the order of 0.998 ± 0.002 . Inner relative transition strengths are normalized to the corresponding brighter outer transition.

	S_1		S_2		S_3		Rel. transition strength	
	Sim.	Expt.	Sim.	Expt.	Sim.	Expt.	Sim.	Expt.
T_1	0.065	0.099 ± 0.010	0	-0.001 ± 0.004	0.998	0.995 ± 0.001	1	1
T_2	-0.223	-0.204 ± 0.001	0	0.001 ± 0.004	0.975	0.979 ± 0.001	0.292	0.296
T_3	-0.223	-0.173 ± 0.001	0	0.015 ± 0.004	-0.975	-0.985 ± 0.001	0.292	0.286
T_4	0.065	0.129 ± 0.008	0	0.016 ± 0.005	-0.998	-0.991 ± 0.001	1	1

Λ -coupled inner transitions in both the oblique and the Voigt configuration using spin pumping as shown in Fig. 3(c). In this section we set out to investigate the spin pumping process in more depth and evaluate the behavior as a function of the resonant laser detuning. Figures 4(a)–4(d) show normalized photon emission count rates, detected at the energy of the transition depicted by the wavy downward arrows, as a function of the laser detuning while the excitation laser is resonantly swept across each transition. The count rate was recorded either with (i) combined application of weak above-band and resonant excitation (Ab.bd+Res.) and (ii) only resonant excitation (Res. only), in order to probe the spin pumping process and the initialization fidelity. In Fig. 4(a) it can be seen that resonantly driving the $|\downarrow\rangle_\theta \rightarrow |\downarrow\uparrow\downarrow\rangle_\theta$ transition (solid red arrow in inset) leads to excitation of the trion state followed by spontaneous decay to one of the two ground states. If the trion decays to the $|\downarrow\rangle_\theta$ state, the resonant laser will simply re-excite it to the trion state. If the decay takes place towards the $|\uparrow\rangle_\theta$ state (wavy black arrow), then the system is initialized

to that state and a photon can be detected at the energy of the $|\downarrow\uparrow\downarrow\rangle_\theta \rightarrow |\uparrow\rangle_\theta$ transition.

If the ground state is long lived, the system remains in this state and the resonant laser has no other effect leading to a measurement of background counts for all resonant laser frequencies. Conversely, using weak above-band excitation enables reshuffling the ground state and therefore the aforementioned process can happen over and over again, leading to a clearly measured spin pumping peak. When resonantly pumping the system, we set the resonant laser power to $P_{\text{Res.}} = 50$ nW and its polarization to linear, to allow for cross-polarized detection. For the weak above-band excitation, we use a linearly polarized laser at 780 nm and set the power to $P_{\text{Ab.bd}} = 6$ nW (approximately 1–1.5% of peak saturation power).

Despite not matching the polarization of the resonant laser (linear) to that of the driven transitions ($\sim 98\%$ circular), we are still able to drive the transitions through the matching circular component of the resonant laser (linear polarization is an equal sum of two cross-circular components).

For further suppression of the resonant laser, we rely on our custom-built double (2×1 m long) Czerny-Turner spectrometer with intermediate slits. By closing the intermediate slits, we only allow photons at the energy of the detected transition to pass through and the combination of intermediate and exit slits gives an overall good suppression. A high contrast between the spin pumping peak and the background counts with only the resonant excitation on is a clear signature of high fidelity initialization. Figures 4(b)–4(d) demonstrate spin pumping through one of the three remaining available transitions in the same manner. This behavior was repeated and consistently observed throughout the sample under the oblique configuration.

It is instructive to compare the spin pumping behavior of this particular quantum dot for oblique fields with spin pumping data from the Voigt configuration which is well understood and has been extensively studied [42–49]. For the spin pumping experiment in the Voigt configuration, we used the same excitation conditions as for the oblique case above. Figures 5(a)–5(d) show spin pumping data for all four transitions in the Voigt configuration. Here, we rotated the excitation/detection polarizations by 90° depending on whether we were pumping the inner [Figs. 5(b) and 5(c)] or the outer [Figs. 5(a) and 5(d)] transitions. A quick comparison between the oblique and Voigt configurations shows a similar behavior with equally high initialization fidelity when resonantly driving the two outer transitions. Upon closer inspection of the spin pumping data when driving the two inner transitions, however, one sees that the background counts in the oblique

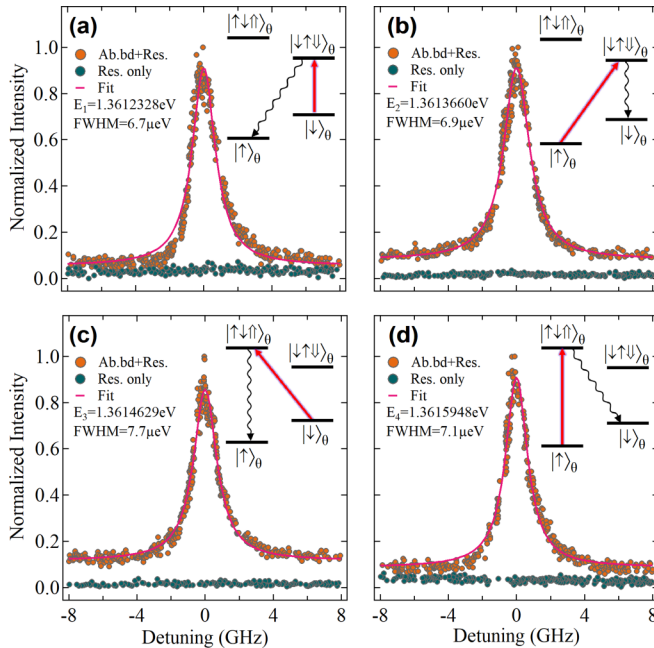


FIG. 4. (a)–(d) Spin pumping of T_1 – T_4 as a function of excitation laser detuning under the oblique configuration. Emission intensity vs single photon counts shown with (i) randomization and (ii) no randomization applied. Solid line is Lorentzian best fit. Inset (top right) shows excitation and detection scheme for each.

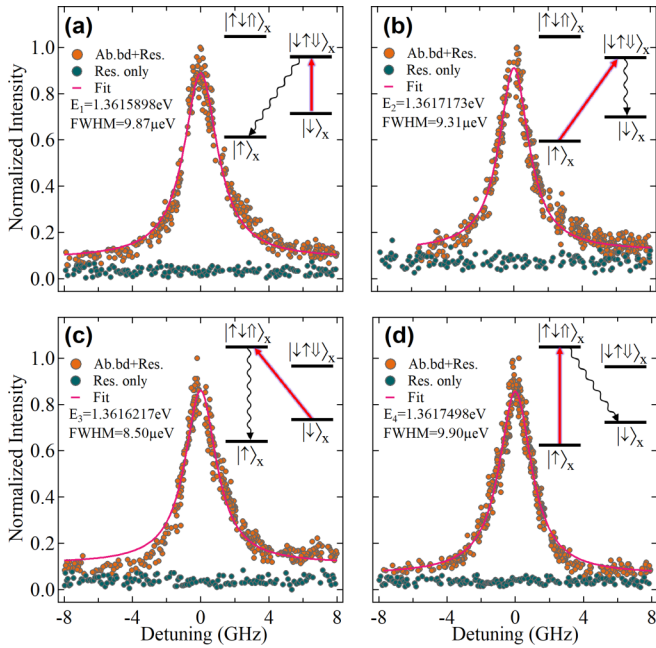


FIG. 5. (a)–(d) Spin pumping of T_1 – T_4 as a function of excitation laser detuning under the Voigt configuration. Emission intensity vs single photon counts shown with (i) randomization and (ii) no randomization applied. Solid line is Lorentzian best fit. Inset (top right) shows excitation and detection scheme for each.

configuration under combined laser excitation away from resonance are higher than the background counts in the Voigt configuration. To understand this one needs to recall that in the oblique case, the two inner transitions have a weaker emission with respect to the outer transitions (~ 0.292 at $\theta_{\text{obl}} = 60^\circ$, $B = 5\text{ T}$). As we are using the same intensity for the above-band laser when driving all four transitions, the PL counts when detecting the outer transitions will be ~ 3.4 times higher than that of the inner transitions.

The comparative study presented here with the similar spin pumping behavior observed for the oblique and Voigt configurations demonstrate that even in oblique fields the tailored ground spin states can be pumped and initialized with high fidelity, a fundamental requirement for quantum information processing applications.

IV. CONCLUSION

In this work, we investigate singly charged QDs under magnetic fields at arbitrary field angles. Using a standard model based on the Luttinger-Kohn Hamiltonian for the heavy holes, we simulate the selection rules and polarization properties of the resulting four-level system. We show that depending on the angle of the oblique magnetic field, we can introduce a controlled spin-state weight imbalance in the ground electron states. This engineered spin composition in the ground states shows promise towards possible applications for spin-selective readout and measurement schemes that are typically employed in the Faraday configuration.

Furthermore, the demonstration of spin pumping and high fidelity initialization of the engineered ground states shows further promise towards demonstration of complete coherent control of the ground states in this configuration, which has direct implications for systems like pyramidal QDs in 1-1-1 GaAs recesses that share the same phenomenology [50,51] but differ in the underlying physics.

ACKNOWLEDGMENTS

The authors thank A. Daley and P. Kirton for fruitful discussions. K.B. acknowledges financial support from the EPSRC Doctoral Training Program under Grant No. EP/R513349/1. S.H. thanks the State of Bavaria for financial support.

- [1] *Semiconductor Quantum Bits*, edited by F. H. Benson Oliver (Jenny Stanford, Singapore, 2011).
- [2] F. P. García de Arquer, D. V. Talapin, V. I. Klimov, Y. Arakawa, M. Bayer, and E. H. Sargent, Semiconductor quantum dots: Technological progress and future challenges, *Science* **373**, 640 (2021).
- [3] *Optical Orientation*, edited by F. Meier and B. P. Zakharchenya (Elsevier, Amsterdam, 1984), Vol. 8.
- [4] E. L. Ivchenko and G. E. Pikus, *Superlattices and Other Heterostructures: Symmetry and Optical Phenomena* (Springer, Berlin, Heidelberg, 1997), Vol. 110.
- [5] P. Y. Yu and M. Cardona, *Fundamentals of Semiconductors: Physics and Materials Properties* (Springer, Berlin, Heidelberg, 2010).
- [6] B. Urbaszek, X. Marie, T. Amand, O. Krebs, P. Voisin, P. Maletinsky, A. Högele, and A. Imamoglu, Nuclear spin physics in quantum dots: An optical investigation, *Rev. Mod. Phys.* **85**, 79 (2013).
- [7] R. J. Warburton, Single spins in self-assembled quantum dots, *Nat. Mater.* **12**, 483 (2013).
- [8] M. Bayer *et al.*, Fine structure of neutral and charged excitons in self-assembled In(Ga)As/(Al)GaAs quantum dots, *Phys. Rev. B* **65**, 195315 (2002).
- [9] J. G. Tischler, A. S. Bracker, D. Gammon, and D. Park, Fine structure of trions and excitons in single GaAs quantum dots, *Phys. Rev. B* **66**, 081310 (2002).
- [10] A. V. Koudinov, I. A. Akimov, Yu. G. Kusrayev, and F. Henneberger, Optical and magnetic anisotropies of the hole states in stranski-krastanov quantum dots, *Phys. Rev. B* **70**, 241305 (2004).
- [11] D. N. Krizhanovskii, A. Ebbens, A. I. Tartakovskii, F. Pulizzi, T. Wright, M. S. Skolnick, and M. Hopkinson, Individual neutral and charged $\text{In}_x\text{Ga}_{1-x}\text{As}$ -GaAs quantum dots with strong in-plane optical anisotropy, *Phys. Rev. B* **72**, 161312 (2005).
- [12] Y. Léger, L. Besombes, L. Maingault, and H. Mariette, Valence-band mixing in neutral, charged, and mn-doped self-assembled quantum dots, *Phys. Rev. B* **76**, 045331 (2007).
- [13] I. Toft and R. T. Phillips, Hole g factors in GaAs quantum dots from the angular dependence of the spin fine structure, *Phys. Rev. B* **76**, 033301 (2007).

- [14] J. Witek, R. W. Heeres, U. Perinetti, E. P. A. M. Bakkers, L. P. Kouwenhoven, and V. Zwiller, Measurement of the g-factor tensor in a quantum dot and disentanglement of exciton spins, *Phys. Rev. B* **84**, 195305 (2011).
- [15] B. Van Hattem, P. Corfdir, P. Brereton, P. Pearce, A. M. Graham, M. J. Stanley, M. Hugues, M. Hopkinson, and R. T. Phillips, From the artificial atom to the kondo-anderson model: Orientation-dependent magneto-photoluminescence of charged excitons in InAs quantum dots, *Phys. Rev. B* **87**, 205308 (2013).
- [16] A. Yugova, A. Greilich, E. A. Zhukov, D. R. Yakovlev, M. Bayer, D. Reuter, and A. D. Wieck, Exciton fine structure in InGaAs–GaAs quantum dots revisited by pump-probe faraday rotation, *Phys. Rev. B* **75**, 195325 (2007).
- [17] A. Schwan, B.-M. Meiners, A. Greilich, D. R. Yakovlev, M. Bayer, A. D. B. Maia, A. A. Quivy, and A. B. Henriques, Anisotropy of electron and hole g-factors in (In, Ga)As quantum dots, *Appl. Phys. Lett.* **99**, 221914 (2011).
- [18] V. V. Belykh, A. Greilich, D. R. Yakovlev, M. Yacob, J. P. Reithmaier, M. Benyoucef, and M. Bayer, Electron and hole g factors in InAs/InAlGaAs self-assembled quantum dots emitting at telecom wavelengths, *Phys. Rev. B* **92**, 165307 (2015).
- [19] V. V. Belykh, D. R. Yakovlev, J. J. Schindler, E. A. Zhukov, M. A. Semina, M. Yacob, J. P. Reithmaier, M. Benyoucef, and M. Bayer, Large anisotropy of electron and hole g factors in infrared-emitting InAs/InAlGaAs self-assembled quantum dots, *Phys. Rev. B* **93**, 125302 (2016).
- [20] S. Varwig, A. Schwan, D. Barmascheid, C. Müller, A. Greilich, I. A. Yugova, D. R. Yakovlev, D. Reuter, A. D. Wieck, and M. Bayer, Hole spin precession in a (In,Ga)As quantum dot ensemble: From resonant spin amplification to spin mode locking, *Phys. Rev. B* **86**, 075321 (2012).
- [21] S. A. Crooker, J. Brandt, C. Sandfort, A. Greilich, D. R. Yakovlev, D. Reuter, A. D. Wieck, and M. Bayer, Spin noise of electrons and holes in self-assembled quantum dots, *Phys. Rev. Lett.* **104**, 036601 (2010).
- [22] J.-M. Meyer, I. Hapke-Wurst, U. Zeitler, R. J. Haug, and K. Pierz, Resonant tunnelling through InAs quantum dots in tilted magnetic fields: Experimental determination of the g-factor anisotropy, *Phys. Status Solidi B* **224**, 685 (2001).
- [23] I. Hapke-Wurst, U. Zeitler, R. J. Haug, and K. Pierz, Mapping the g factor anisotropy of InAs self-assembled quantum dots, *Physica E* **12**, 802 (2002).
- [24] T. P. M. Alegre, F. G. G. Hernández, A. L. C. Pereira, and G. Medeiros-Ribeiro, Landé g tensor in semiconductor nanostructures, *Phys. Rev. Lett.* **97**, 236402 (2006).
- [25] C. A. Jiménez-Orjuela, H. Vinck-Posada, and M. J. Villas-Bôas, Dark excitons in a quantum-dot–cavity system under a tilted magnetic field, *Phys. Rev. B* **96**, 125303 (2017).
- [26] M. Neumann, F. Kappe, T. K. Bracht, M. Cosacchi, T. Seidelmann, V. M. Axt, G. Weihs, and D. E. Reiter, Optical stark shift to control the dark exciton occupation of a quantum dot in a tilted magnetic field, *Phys. Rev. B* **104**, 075428 (2021).
- [27] Z. Zeng, C. S. Garoufalidis, S. Baskoutas, and A. F. Terzis, Tuning the binding energy of surface impurities in cylindrical GaAs/AlGaAs quantum dots by a tilted magnetic field, *J. Appl. Phys.* **112**, 064326 (2012).
- [28] C. Heyn and C. A. Duque, Donor impurity related optical and electronic properties of cylindrical GaAs–Al_xGa_{1-x}As quantum dots under tilted electric and magnetic fields, *Sci. Rep.* **10**, 9155 (2020).
- [29] J. Debus, V. F. Sapega, D. Dunker, D. R. Yakovlev, D. Reuter, A. D. Wieck, and M. Bayer, Spin-flip raman scattering of the resident electron in singly charged (In,Ga)As/GaAs quantum dot ensembles, *Phys. Rev. B* **90**, 235404 (2014).
- [30] J. Debus, T. S. Shamirzaev, D. Dunker, V. F. Sapega, E. L. Ivchenko, D. R. Yakovlev, A. I. Toropov, and M. Bayer, Spin-flip raman scattering of the Γ -X mixed exciton in indirect band gap (In, Al)As/AlAs quantum dots, *Phys. Rev. B* **90**, 125431 (2014).
- [31] C. Tonin, R. Hostein, V. Voliotis, R. Grousson, A. Lemaitre, and A. Martinez, Polarization properties of excitonic qubits in single self-assembled quantum dots, *Phys. Rev. B* **85**, 155303 (2012).
- [32] An additional polarimetry experiment was performed for this purpose in Faraday geometry (not shown) and both visible transitions showed a very high degree of circular polarization $|S_3| \geq 0.9994 \pm 0.0007$.
- [33] H. G. Berry, G. Gabrielse, and A. E. Livingston, Measurement of the stokes parameters of light, *Appl. Opt.* **16**, 3200 (1977).
- [34] B. Schaefer, E. Collett, R. Smyth, D. Barrett, and B. Fraher, Measuring the stokes polarization parameters, *Am. J. Phys.* **75**, 163 (2007).
- [35] T. Karin, R. J. Barbour, C. Santori, Y. Yamamoto, Y. Hirayama, and K.-M. C. Fu, Radiative properties of multicarrier bound excitons in GaAs, *Phys. Rev. B* **91**, 165204 (2015).
- [36] S. Maier, P. Gold, A. Forchel, N. Gregersen, J. Mørk, S. Höfling, C. Schneider, and M. Kamp, Bright single photon source based on self-aligned quantum dot–cavity systems, *Opt. Express* **22**, 8136 (2014).
- [37] D. Press, K. De Greve, P. L. McMahon, T. D. Ladd, B. Friess, C. Schneider, M. Kamp, S. Höfling, A. Forchel, and Y. Yamamoto, Ultrafast optical spin echo in a single quantum dot, *Nat. Photon.* **4**, 367 (2010).
- [38] K. Barr, T. Cookson, and K. G. Lagoudakis, Operation of a continuous flow liquid helium magnetic microscopy cryostat as a closed cycle system, *Rev. Sci. Instrum.* **92**, 123701 (2021).
- [39] T. A. Wilkinson, C. E. Maurer, C. J. Flood, G. Lander, S. Chafin, and E. B. Flagg, Complete stokes vector analysis with a compact, portable rotating waveplate polarimeter, *Rev. Sci. Instrum.* **92**, 093101 (2021).
- [40] S. G. Reddy, S. Prabhakar, A. Aadhi, A. Kumar, M. Shah, R. P. Singh, and R. Simon, Measuring the mueller matrix of an arbitrary optical element with a universal SU(2) polarization gadget, *J. Opt. Soc. Am. A* **31**, 610 (2014).
- [41] See Supplemental Material at <http://link.aps.org/supplemental/10.1103/PhysRevB.109.075433> for above-band saturation power curve.
- [42] X. Xu, Y. Wu, B. Sun, Q. Huang, J. Cheng, D. G. Steel, A. S. Bracker, D. Gammon, C. Emary, and L. J. Sham, Fast spin state initialization in a singly charged InAs–GaAs quantum dot by optical cooling, *Phys. Rev. Lett.* **99**, 097401 (2007).
- [43] C. Emary, X. Xu, D. G. Steel, S. Saikin, and L. J. Sham, Fast initialization of the spin state of an electron in a quantum dot in the voigt configuration, *Phys. Rev. Lett.* **98**, 047401 (2007).
- [44] V. Loo, L. Lanco, O. Krebs, P. Senellart, and P. Voisin, Single-shot initialization of electron spin in a quantum dot using a short optical pulse, *Phys. Rev. B* **83**, 033301 (2011).
- [45] K. G. Lagoudakis, K. A. Fischer, T. Sarmiento, K. Mueller, and J. Vučković, Hole-spin pumping and repumping in a p-Type δ -doped InAs quantum dot, *Phys. Rev. B* **90**, 121402 (2014).

- [46] B. D. Gerardot, D. Brunner, P. A. Dalgarno, P. Öhberg, S. Seidl, M. Kroner, K. Karrai, N. G. Stoltz, P. M. Petroff, and R. J. Warburton, Optical pumping of a single hole spin in a quantum dot, *Nature* **451**, 441 (2008).
- [47] K. G. Lagoudakis *et al.*, Initialization of a spin qubit in a site-controlled nanowire quantum dot, *New J. Phys.* **18**, 053024 (2016).
- [48] M. Atatüre, J. Dreiser, A. Badolato, A. Högele, K. Karrai, and A. Imamoglu, Quantum-dot spin-state preparation with near-unity fidelity, *Science* **312**, 551 (2006).
- [49] M. Kroner, K. M. Weiss, B. Biedermann, S. Seidl, A. W. Holleitner, A. Badolato, P. M. Petroff, P. Öhberg, R. J. Warburton, and K. Karrai, Resonant two-color high-resolution spectroscopy of a negatively charged exciton in a self-assembled quantum dot, *Phys. Rev. B* **78**, 075429 (2008).
- [50] G. Sallen *et al.*, Dark-bright mixing of interband transitions in symmetric semiconductor quantum dots, *Phys. Rev. Lett.* **107**, 166604 (2011).
- [51] M. V. Durnev *et al.*, Magnetic field induced valence band mixing in [111]grown semiconductor quantum dots, *Phys. Rev. B* **87**, 085315 (2013).